1 **Measurement report: Molecular-level investigation of**

2 **atmospheric cluster ions at the tropical high-altitude research**

3 **station Chacaltaya (5240 m a.s.l.) in the Bolivian Andes**

4 Qiaozhi Zha[1], Wei Huang[1*], Diego Aliaga[1], Otso Peräkylä[1], Liine Heikkinen[2], Alkuin

5 Maximilian Koenig[3], Cheng Wu[4], Joonas Enroth[1], Yvette Gramlich[2], Jing Cai[1], Samara

6 Carbone[5], Armin Hansel[6], Tuukka Petäjä[1], Markku Kulmala[1,7,8], Douglas Worsnop[1,9],

7 Victoria Sinclair[1], Radovan Krejci[2], Marcos Andrade[10,11], Claudia Mohr[2], Federico

8 Bianchi[1*]

9 *[1] Institute for Atmospheric and Earth System Research /Physics, University of Helsinki,*

10 *Helsinki, Finland*

11 *[2] Department of Environmental Science & Bolin Centre for Climate Research, Stockholm*

12 *University, Stockholm, Sweden*

13 *[3] Institut des Géosciences de l'Environnement, Univ Grenoble Alpes, CNRS, IRD, Grenoble*

14 *INP, Grenoble, France*

15 *[4] Department of Chemistry & Molecular Biology, University of Gothenburg, Sweden*

16 *[5] Federal University of Uberlândia, Uberlândia, MG, Brazil*

17 *[6] Institute for Ion and Applied Physics, University of Innsbruck, Innsbruck, Austria*

18 *[7] Joint International Research Laboratory of Atmospheric and Earth System Sciences, Nanjing*

19 *University, Nanjing, China*

20 *[8] Aerosol and Haze Laboratory, Beijing Advanced Innovation Center for Soft Matter Science*

21 *and Engineering, Beijing University of Chemical Technology, Beijing, China*

22 *[9] Aerodyne Research, Inc., Billerica, MA, USA*

23 *[10] Laboratory for Atmospheric Physics, Institute for Physics Research, Universidad Mayor de*

24 *San Andrés, La Paz, Bolivia*

25 *[11] epartment of Atmospheric and Oceanic Sciences, University of Maryland, College Park, MD,*

26 *USA*

27 *Corresponding author*: Wei Huang, wei.huang@helsinki.fi and Federico Bianchi,

28 federico.bianchi@helsinki.fi

29

Abstract

30

31 Air ions are the key components for a series of atmospheric physicochemical
32 interactions, such as ion-catalyzed reactions, ion-molecule reactions, and ion-induced
33 new particle formation. They also control atmospheric electrical properties with effects
34 on global climate. We performed molecular-level measurements of cluster ions at the
35 high-altitude research station Chacaltaya (CHC; 5240 m a.s.l.), located in the Bolivian
36 Andes, from January to May 2018 using an atmospheric pressure interface time-of-
37 flight mass spectrometer. The negative ions mainly consisted of $(H_2SO_4)_{0-3} \cdot HSO_4^-$,
38 $(HNO_3)_{0-2} \cdot NO_3^-$, SO_5^-, $(NH_3)_{1-6} \cdot (H_2SO_4)_{3-7} \cdot HSO_4^-$, malonic acid-derived, and
39 $CHO/CHON \cdot (HSO_4^-/NO_3^-)$ cluster ions. Their temporal variability exhibited distinct
40 diurnal and seasonal patterns due to the changes in the corresponding neutral species'
41 molecular properties (such as electron affinity and proton affinity) and concentrations
42 resulting from the air masses arriving at CHC from different source regions. The
43 positive ions were mainly composed of protonated amines and organic cluster ions, but
44 exhibited no clear diurnal variation. H_2SO_4-NH_3 cluster ions likely contributed to the
45 new particle formation process, particularly during wet-to-dry transition period and dry
46 season when CHC was more impacted by air masses originating from source regions
47 with elevated SO_2 emissions. Our study provides new insights into the chemical
48 composition of atmospheric cluster ions and their role in new particle formation in the
49 high-altitude mountain environment of the Bolivian Andes.

1 Introduction

50

51 Air ions regulate the electrical properties of the atmosphere by serving as carriers of
52 electrical charges (Williams, 2009). They also play an important role in atmospheric
53 chemistry by participating/catalyzing ion-molecule reactions and ion-induced new
54 particle formation (NPF, Hirsikko et al., 2011). The formation of tropospheric ions is
55 initiated through simple-structured ions, such as O^+, N_2^+, O^-, and O_2^-, mainly from
56 radioactive decay in the soil (e.g., radon and gamma radiation), thunderstorm activity
57 (lightning), and galactic cosmic rays (GCR). These ions can transfer their charges to
58 other compounds, leading to the subsequent production of an assortment of ions, such
59 as the bisulfate ion (HSO_4^-), nitrate ion (NO_3^-), hydronium ion (H_3O^+), and ammonium
60 ion (NH_4^+; Smith and Spanel, 1995; Hirsikko et al., 2011). Depending on their sizes,
61 air ions are usually classified into cluster ions (diameter $\leq$ 1.6 nm) that are charged
62 molecules or molecular clusters, and charged particles (diameter > 1.6 nm; Hirsikko et
63 al., 2005, 2011; Komppula et al., 2007).

64 Cluster ions exist almost always in the troposphere and can undergo frequent ion-
65 molecule reactions during their lifetime (~100 seconds; Manninen et al., 2010; Hirsikko
66 et al., 2011). Their chemical composition, in addition to the initial ionization, also
67 depends on the concentrations of the parent neutral species (Eisele, 1986). Bianchi et
68 al. (2017) showed that the diurnal cycle of negative organic ions followed the variations
69 of their neutral molecules' concentrations in a boreal forest, since the higher

70 concentrations of neutral molecules would result in a larger probability of them being
71 charged. Moreover, molecular properties of the neutral species, such as electron affinity
72 (EA) and proton affinity (PA), are also important for determining cluster ion
73 composition. Cluster ions derived from molecules with higher EA (e.g., HSO_4 and NO_3)
74 or PA (e.g., trimethylamine (C_3H_9N) and pyridine (C_5H_5N)) tend to obtain the ambient
75 negative or positive charge, respectively (Ferguson and Arnold, 1981; Hirsikko et al.,
76 2011). Because of the strong EA or PA, it is almost unlikely that the ions derived from
77 those molecules will further transfer their charges to other neutral compounds via ion-
78 molecule reactions. Thus, these negative (HSO_4^- and NO_3^-) and positive ($C_3H_{10}N^+$ and
79 $C_5H_6N^+$) ions are usually more abundant than other ions in the atmosphere (Eisele, 1986;
80 Ehn et al., 2010; Bianchi et al., 2017; Frege et al., 2017). In contrast, charge transfer
81 occurs more easily for ions derived from neutral species of lower EA or PA.

82 Atmospheric cluster ions can contribute to new particle formation (NPF) via ion-
83 induced nucleation (Yu, 2010). Since the discovery of this mechanism in the first cloud
84 chamber study in the early 1900s (Wilson, 1911), ion-induced nucleation has been
85 known as an important source of atmospheric aerosol particles. Recently, a series of
86 chamber studies conducted at the CLOUD (Cosmics Leaving Outdoor Droplets) facility
87 at CERN (the European Centre for Nuclear Research) have shown that aerosol
88 nucleation rates are substantially enhanced in the presence of some specific cluster ions,
89 such as sulfuric acid – ammonia (H_2SO_4 – NH_3) cluster ions (Kirkby et al., 2011;
90 Schobesberger et al., 2015), pure H_2SO_4 cluster ions (Kirkby et al., 2011), and organic
91 cluster ions (Kirkby et al., 2016). Field measurements have also suggested the important
92 role of atmospheric ions in ion-induced nucleation (Manninen et al., 2010; Hirsikko et
93 al., 2011; Rose et al., 2018; Jokinen et al., 2018; Yan et al., 2018; Beck et al., 2021).
94 Among them, the onsets of high-altitude NPF events, compared to those occurring in
95 the lower troposphere, are often associated with more abundant cluster ions (Lee et al.,
96 2003; Venzac et al., 2008; Boulon et al., 2010). Such increases are due to the higher
97 GCR intensity and lower condensation sink (CS) in the high-altitude regions. As a result,
98 potentially larger contributions of cluster ions to aerosol formation would be expected
99 (Smith and Spanel, 1995; Hirsikko et al., 2011).

100 However, the molecular-level understanding of ambient cluster ions and their influence
101 on NPF in high-altitude environments (in the troposphere) is still very limited. Two
102 mountaintop studies in the Alps show that, depending on the air mass origins, NPF
103 could be triggered by sulfuric acid-ammonia clusters, or nitrate (or sulfuric acid)
104 clustering with highly oxygenated organic molecules (Bianchi et al., 2016; Frege et al.,
105 2017). Another study in the Himalayas found that NPF was mainly driven by organic
106 vapors of biogenic origin (Bianchi et al., 2021). Recently, frequent and intensive NPF
107 events were observed at the high-altitude research station Chacaltaya (CHC; 16.3505°
108 S, 68.1314° W; 5240 m a.s.l.) located in the Bolivian Andes (Rose et al., 2015), but the
109 exact mechanism and the role of cluster ions in aerosol nucleation process remain
110 unclear. Therefore, a detailed investigation of cluster ions at CHC, including their

111   molecular composition, temporal variation (diurnal and seasonal), and source regions,
112   is needed in order to understand their role in atmospheric processes such as NPF in the
113   study regions.

114   Here we present measurements of atmospheric ions from January to May 2018 at CHC.
115   The dataset is part of the Southern hemisphere high ALTitude Experiment on particle
116   Nucleation And growth (SALTENA) field experiment campaign (Bianchi et al., 2022).
117   During the study period, the sampled air masses originated from various source regions,
118   such as the Amazon Basin to the east and the Altiplano and the Pacific Ocean to the
119   west (Fig. 1a; Aliaga et al., 2021). Temporal evolution (diurnal and/or seasonal
120   variations) of both negative and positive ion composition are investigated, and their
121   potential connections with source regions and NPF are discussed. Our study thus adds
122   important observational information on a better understanding of atmospheric ions and
123   provides new insights into their role in high-altitude NPF in the troposphere of the
124   Bolivian Andes.

125   **2   Methods**

126   **2.1 Measurement site description**

127   The high-altitude research station CHC is ~140 m below the summit of Mount
128   Chacaltaya (5380 m a.s.l.) with an open view to the south and west (Andrade et al.,
129   2015). The La Paz – El Alto metropolitan area (with 1.7 million inhabitants) is ~1 – 1.6
130   km lower (in altitude) and ~15 km south of CHC (Fig. 1b). The seasonal meteorological
131   conditions at CHC depend on the cycle between the wet (November to March; wet-to-
132   dry transition period in April) and dry (May to September; dry-to-wet transition period
133   in October) seasons driven by large-scale tropical circulation (Rose et al., 2015; Bianchi
134   et al., 2022). This pattern also affects the source regions of air masses arriving at CHC
135   (Aliaga et al., 2021). Additionally, due to the strong diurnal cycle of the planetary
136   boundary layer (PBL) height and the thermally-induced winds in the mountainous
137   terrain, CHC is often affected by polluted PBL transported from the La Paz – El Alto
138   metropolitan area during daytime (Wiedensohler et al., 2018) whereas at night CHC is
139   located in the residual layer or tropical free troposphere (Coen et al., 2018).
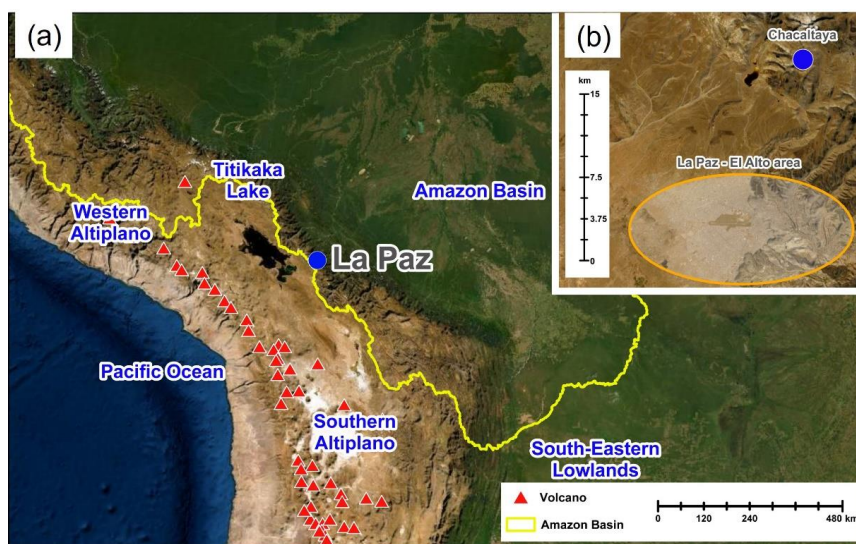
Figure 1 **(a)** True-color satellite image showing the location of CHC (blue circle) and its surrounding area. The yellow line presents the boundary of the Amazon Basin. Red triangles denote the volcanoes in this area. **(b)** A zoomed-in true-color satellite image showing the distance between CHC and the La Paz – El Alto metropolitan area (orange circle). Image sources: Esri, DigitalGlobe, GeoEye, i-cubed, USDA FSA, USGS, AEX, Getmapping, Aerogrid, IGN, IGP, swisstopo, and the GIS User Community.

2.2 Instrumentation

All the instruments involved in this study were installed in a temperature-controlled measurement room (at ~25 °C). All data are reported in local time (UTC-4).

2.2.1   Measurements of atmospheric cluster ions

The composition of cluster ions was measured by an atmospheric pressure interface time-of-flight mass spectrometer (APi-TOF, Aerodyne Research Inc. & Tofwerk AG). The APi-TOF consists of an atmospheric pressure interface (APi) module and a time-of-flight (TOF) mass spectrometer. The APi module allows the instrument to sample ions from ambient air directly. The positive or negative ions within the sampled airflow are focused and guided by two quadrupoles and an ion lens, with a gradually decreasing pressure (from atmospheric pressure to ~10^{-4} mbar), before entering the TOF mass spectrometer (~10^{-6} mbar). A more detailed description of this instrument is given in Junninen et al. (2010). In this study, ambient air was sampled through a ~1.5 m stainless steel tube with a total sample flow of 14 standard liters per minute (SLPM) to ensure laminar flow during sampling, and 0.8 SLPM of the total flow entered the APi-TOF.

During the wet season, the APi-TOF was first operated in negative mode to measure negative cluster ions (January), and then switched to positive mode to measure positive cluster ions (February to March). During the wet-to-dry transition period (April) and

164 dry season (May), the instrument was changed back to negative mode to investigate the
165 potential seasonality of negative ion composition. It is important to note that, similar to
166 Frege et al. (2017), for better characterization of the connection between cluster ions
167 and NPF, we only included the ion data from cloud-free days in this study (to avoid
168 influence from, e.g., lightning activity).

2.2.2   Measurements of H_2SO_4 and oxidized organic molecules

170 Concentrations of H_2SO_4 and oxidized organic molecules (OOM) were measured using
171 a nitrate ion (NO_3^-) based chemical ionization atmospheric pressure interface time-of-
172 flight mass spectrometer (CI-APi-TOF, Aerodyne Research Inc. & Tofwerk AG;
173 Jokinen et al., 2012). The instrument is a combination of the APi-TOF and a chemical
174 ionization (CI) unit, which has been widely used to measure H_2SO_4 in the atmosphere
175 (Jokinen et al., 2012; Bianchi et al., 2016; Zha et al., 2018). In this study, a soft X-ray
176 source (L9490, Hamamatsu) was used to charge nitric acid (HNO_3) in a sheath flow of
177 20 SLPM to produce the reagent ion, NO_3^-. H_2SO_4 and OOM in the sample flow (10
178 SLPM) were then charged by either proton transfer or the formation of an adduct with
179 the reagent ion during the ~200 ms residence time in the CI unit. A calibration factor of
180 1.5×10^{10} cm^{-3} for H_2SO_4 was determined (with sampling loss corrected) according to
181 the approach by Kürten et al. (2012). The same calibration coefficient was adopted for
182 determining OOM concentrations in this study, which could result in an
183 underestimation of their concentrations due to a lower charging efficiency of OOM than
184 H_2SO_4 by NO_3^- (Hyttinen et al., 2015).

2.2.3   Auxiliary measurements

186 The number concentration and size distribution of atmospheric ions and neutral
187 particles were measured with a neutral cluster and air ion spectrometer (NAIS, Airel
188 Ltd., Mirme and Mirme, 2013). The instrument can detect air ions with a diameter from
189 1.4 to 50 nm, including both cluster ions and charged particles. The details of the
190 instrument used can be found in Rose et al. (2017).

191 Particle number size distributions between 10 to 500 nm were measured by a Mobility
192 Particle Size Spectrometer (MPSS; Wiedensohler et al., 2012), and the data was used
193 for calculating the CS, which represents the loss rate of condensing vapors and cluster
194 ions on pre-existing particles (Kulmala et al., 2001).

195 Meteorological parameters, such as temperature, relative humidity (RH), and global
196 radiation, were also measured simultaneously at CHC. Detailed descriptions can be
197 found in Bianchi et al. (2022).

2.3 Simulation of air mass origin and history

199 To understand the source regions and transport pathways of the air masses arriving at
200 CHC, we used the results of air mass history analysis obtained from FLEXPART-WRF
201 simulations described in Aliaga et al. (2021). In brief, a Lagrangian transport and

202 dispersion model (FLEXPART-WRF; version 3.3.2; Brioude et al., 2013) was used to
203 calculate the air mass history during the campaign period. The backward simulation
204 was driven by the high spatial and temporal resolution meteorological output from the
205 Weather Research and Forecasting model (WRF; version 4.0.3; Skamarock et al., 2019).
206 In the simulation, twenty thousand particles were continuously released every hour
207 from a 10 m deep layer (0 – 10 m a.g.l.) at CHC and traced back in the atmosphere for
208 96 hours. The output of the FLEXPART-WRF is the source-receptor relationship (SRR,
209 in seconds), which is calculated for each geographical grid cell included in the
210 simulation. The SRR value depends on the particle's residence time and the number of
211 particles in the output grid cells. Clustering analysis was conducted by applying a series
212 of pretreatments (e.g., log-polar grid transformation and grid cell pre-processing) and a
213 k-means clustering algorithm (Lloyd, 1982) to the calculated SSR dataset (see Aliaga
214 et al. (2021) for more details).

2.3.1 Major air mass pathways

216 Six air mass pathways (PW) representing air masses arriving at CHC were determined
217 from the clustering analysis. They are named based on their clock positions from CHC
218 (e.g., 03_PW indicates the pathway with its centroid located at the 3 o'clock direction
219 (east, 90°) of CHC, Fig. 2a). Characteristics of these air mass pathways, such as source
220 region, transport distance, and transport time, were distinct from each other (Table 1).
221 A detailed description of the air mass pathways and their characteristics can be found
222 in Aliaga et al. (2021).

223 The influence of each air mass pathway on CHC varied with time, and was estimated
224 by its SRR percentage ($SRR[\%]_{pathway}$) as in equation (1):

$$SRR[\%]_{pathway} = \frac{SRR_{pathway}}{SRR_{total}} \times 100 \qquad (1)$$

226 where $SRR_{pathway}$ and SRR_{total} are the residence time of a specific air mass pathway and
227 in total (96 hours = 345600 seconds) in the simulation, respectively.

228 Table 1. Overview of the six air mass pathways extracted from Aliaga et al. (2021).

| Pathway	Direction to CHC	Representative source region	Transport distance (km)[1] Median (25 – 75 %)	Transport time (hour) Median (25 – 75 %)
03_PW	East	Amazon Basin and Eastern/South-Eastern Lowlands	518 (413–608)	51 (45-57)
05_PW	South and Southeast	South-Eastern Lowlands and Southern Altiplano	428 (303-567)	45 (36-52)
07_PW	Southwest	The Pacific Ocean, coastal area, Western Altiplano, and La Paz – El Alto	721 (577-896)	54 (45-61)
08_PW	West	Western Altiplano and	238 (198-279)	36 (29-43)

		Titicaca lake, coastal area		
11_PW	North and Northwest	Amazon Basin, Western Altiplano, coastal area	465 (326-563)	53 (46-59)
12_PW	North	Amazon Basin	76 (49 -95)	27 (21-33)

229 [1]Distance between CHC and each pathway's center point (see Fig. 2a).

2.3.2   Identification of representative periods for each air mass pathway

Air mass history analysis shows that the air sampled at CHC was typically a mixture of multiple pathways. Thus, the cluster ion composition observed during the study period was often influenced by multiple source regions concurrently. To characterize the influence of every single pathway on cluster ion composition, periods when an air mass pathway exerted its largest impact on CHC (the highest 10% of its SRR[%]$_{pathway}$ values; Fig. 2b) during the whole study period are identified as the representative periods of the specific pathway. For instance, the representative periods of 03_PW (covering, e.g., the Amazon Basin) are more frequently seen during wet season (highest in January), whereas 08_PW (covering, e.g., Altiplano region) has most of its representative periods in dry season (highest in May). Note that SRR[%]$_{pathway}$ of any individual pathway rarely reached 40 % during the whole study period (see Fig. S1), and thus the representative periods cannot be directly identified via SRR[%]$_{pathway}$ values (e.g., using a certain threshold of the value) as in a previous study (Koenig et al., 2021).
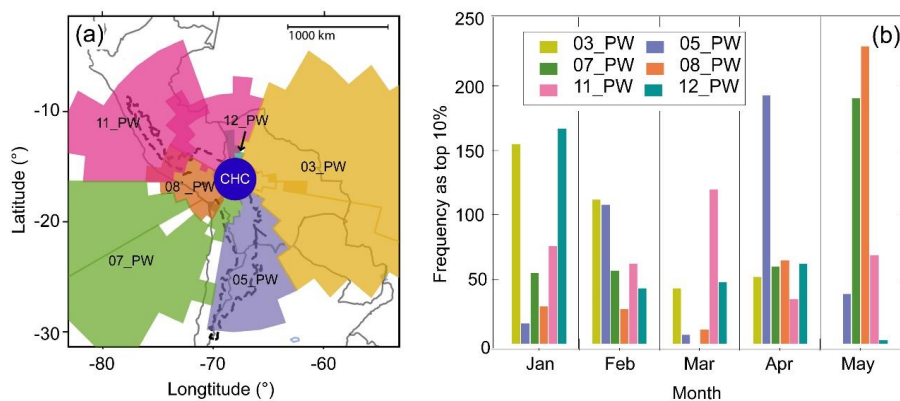
Figure 2 Influence of the six air pathways on CHC from January to May 2018. **(a)** Horizontal profile of the air mass pathways, adapted from Aliaga et al. (2021). **(b)** Frequency of the representative periods for each pathway (the highest 10% of their corresponding SRR[%]$_{pathway}$) in different months.

## 3   Results and discussion

3.1 Variation in total ion count

During the study period, the total ion count (TIC) observed by APi-TOF at CHC varied

252 between <10 and 100 counts per second (cps; Fig. 3 and Fig. S2). Similar variations in
253 the TIC were also observed in the long-term cluster ion measurements at the high-
254 altitude station Jungfraujoch in Switzerland (JFJ; 3454 m a.s.l.; Frege et al., 2017) and
255 were attributed to the seasonal changes of ion precursor and sink. Like the winter–
256 summer seasonality of the JFJ, CHC and its adjacent mountain areas are frequently
257 covered by snow in wet season and mostly free of snow in dry season (Bianchi et al.,
258 2022; Koenig et al., 2021). Thus, in contrast with the generally stable GCR flux
259 (primarily controlled by the decadal scale solar cycle; Shuman et al., 2015), a reduced
260 radioactive decay from the soil and a lower ion production rate could be expected at
261 CHC in wet season than in dry season.

262 However, the TIC measured by APi-TOF was significantly higher in wet season ($41 \pm$
263 23 cps, mean $\pm$ standard deviation) and the wet-to-dry transition period (56 ± 32 cps)
264 than in dry season (14 ± 11 cps; Fig. S2). Considering the slight negative correlation
265 (Pearson's correlation coefficient (R): -0.41; Fig. 3) between the TIC and CS
266 (representing the loss rate of condensing vapors and cluster ions on pre-existing
267 particles; Kulmala et al., 2001), the observed TIC fluctuation may be related (at least
268 partially) to the varying CS ($\sim 1 \times 10^{-4}$ s^{-1} in wet season to $\sim 5 \times 10^{-2}$ s^{-1} in the dry season).
269 Moreover, the cluster ions measured by APi-TOF usually account for only a small
270 fraction of the total atmospheric ions (Rose et al., 2018). Changes in the fraction of
271 small ions in total atmospheric ions can potentially lead to a fluctuation in TIC (Frege
272 et al., 2017). This is illustrated in Figure 3 that a smaller TIC determined from APi-TOF
273 is associated with a lower fraction of smaller ions (< 2 nm) observed by NAIS (mostly
274 cluster ions). However, for better characterization of the influences of different ion
275 composition on CHC and their diurnal and seasonal relative changes, we normalized
276 the observed ion signal to the TIC for APi-TOF measurements.

277
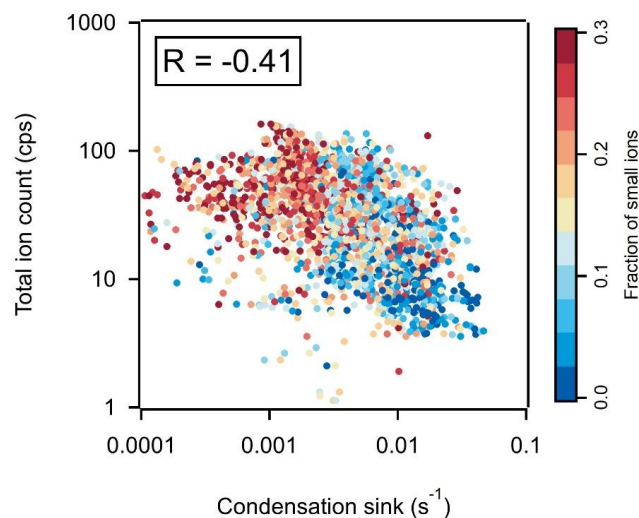
Figure 3 Correlation between the TIC measured by APi-TOF and condensation sink, colored by the fraction of small ions (defined as concentrations of ions with diameter <2 nm to the total ion concentrations) determined from NAIS data. Data are shown in the time resolution of 1 hour.

3.2 Negative ions

3.2.1 Main negative ions and their diurnal variation

A number of negative ions were consistently observed at CHC throughout the study period (i.e., in the wet, wet-to-dry transition, and dry seasons). Based on the chemical composition of the observed negative ions, we classified them into eight groups as follows: sulfuric acid ($(H_2SO_4)_{0-3} \cdot HSO_4^-$), nitric acid ($(HNO_3)_{0-2} \cdot NO_3^-$), SO_5^-, sulfuric acid-ammonia ($(NH_3)_{1-6} \cdot (H_2SO_4)_{3-7} \cdot HSO_4^-$), malonic acid-derived (MA-derived; including $C_3H_3O_4^-$, $C_3H_4O_4 \cdot NO_3^-$, and $C_3H_4O_4 \cdot HSO_4^-$), oxidized organic molecules ($CHO/CHON \cdot (HSO_4^-/NO_3^-)$), others (other identified negative ions, such as IO_3^-), and unidentified ions. The campaign-average diurnal variations of these eight negative ion groups are shown in Figure 4. Different diurnal patterns of each negative ion group were observed, mainly due to changes in concentrations of the parent neutral species and their unique physicochemical properties (e.g., the EA and PA of molecules; Ferguson and Arnold, 1981; Bianchi et al., 2017; Hirsikko et al., 2011).

$(HNO_3)_{0-1} \cdot NO_3^-$ and $(H_2SO_4)_{0-3} \cdot HSO_4^-$ were among the highest in the signal of all negative ion groups in all seasons, making up 37 % (whole day) and 20 % (daytime; 07:00 – 19:00, and hereafter) of negative ions at CHC during the study period, respectively. The EA of their neutral molecules (HSO_4 and NO_3) is higher than that of most of the neutral species in the atmosphere, and thus hinders the direct electron transfer from HSO_4^- and NO_3^- to other molecules through ion-molecule reactions (Ferguson and Arnold, 1981). As a result, these ion groups were found to dominate

302 negative cluster ions at CHC and also other locations, such as a number of remote sites
303 in the United States (Eisele, 1986), a boreal forest site in Finland (Ehn et al., 2010;
304 Bianchi et al., 2017), and the JFJ in Switzerland (Frege et al., 2017).

305 Distinct diurnal patterns were observed for the $(HNO_3)_{0-1} \cdot NO_3^-$ and $(H_2SO_4)_{0-3} \cdot HSO_4^-$
306 ion groups. $(HNO_3)_{0-1} \cdot NO_3^-$ exhibited a relatively flat diurnal pattern (see Fig. 4) with
307 similar fractions at daytime (35 %) and nighttime (19:00 – 07:00; 39 %). Such a diurnal
308 pattern could result from the high EA of the NO_3 molecule (4.01 eV and an additional
309 ~1 eV per HNO_3; Ferguson and Arnold, 1981), and its relatively abundant (usually
310 several ppbv) parent neutral species (e.g., HNO_3 and N_2O_5) with multiple sources in the
311 atmosphere (e.g., anthropogenic emission and lightning; Martin et al., 2007). In contrast,
312 $(H_2SO_4)_{0-3} \cdot HSO_4^-$ exhibited a strong diurnal variation. While the fraction of $(H_2SO_4)_{0-3} \cdot HSO_4^-$
313 remained low (2 %) during nighttime, it started to increase after sunrise (shortly
314 after 07:00) and reached a maximum (30 %) at around 10:00. Despite an EA comparable
315 to that of the NO_3 molecule (4.75 eV for HSO_4; Wang et al., 2000), the strong diurnal
316 variation of $(H_2SO_4)_{0-3} \cdot HSO_4^-$ is a result of the photochemical production of neutral
317 H_2SO_4. The influence of neutral H_2SO_4 on $(H_2SO_4)_{0-3} \cdot HSO_4^-$ is indicated by their
318 similar diurnal patterns (R: 0.52; see Fig. S3a). Similarly, a higher level of $(NH_3)_{1-6} \cdot (H_2SO_4)_{3-7} \cdot HSO_4^-$ was only observed with the presence of abundant $(H_2SO_4)_{0-3} \cdot HSO_4^-$
320 during daytime. It is also important to note that the decreases of $(H_2SO_4)_{0-3} \cdot HSO_4^-$ and
321 $(NH_3)_{1-6} \cdot (H_2SO_4)_{3-7} \cdot HSO_4^-$ at around noontime (12:00; see Fig. 4) coincided with an
322 enhanced CS, indicating the influence of a higher ion sink in addition to the decrease
323 in neutral H_2SO_4 concentration (Boulon et al., 2010; Frege et al., 2017).
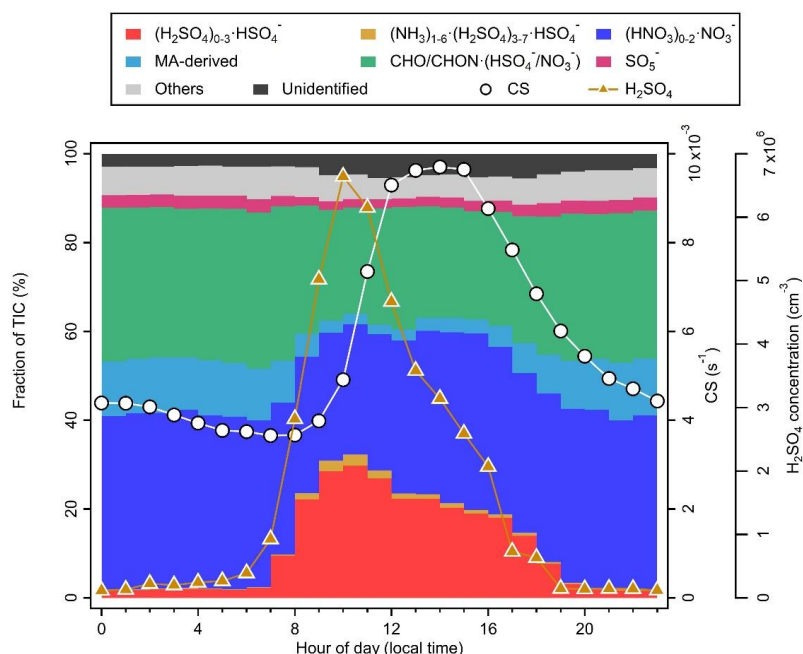
Figure 4 Diurnal variation of the negative ions (fraction of TIC), CS, and neutral H_2SO_4 concentrations at CHC, averaged over the periods when negative ions were measured (i.e., January, April, and May 2018).

The MA-derived ion group is distinguished from the $CHO/CHON \cdot (HSO_4^-/NO_3^-)$ ion group due to its abundance in total organic ions. This group of ions, mainly composed of $C_3H_3O_4^-$, is formed from the deprotonation of malonic acid, with a higher EA (~4.60 eV) than that of the NO_3 molecule (4.01 eV; Ravi Kumar et al., 2005). Thus, the fraction of the MA-derived ion group was high during nighttime (12 %; see Fig. 4). In contrast, its fraction decreased significantly (to 5 %) during daytime due to the increase of $(H_2SO_4)_{0-3} \cdot HSO_4^-$, which has an even higher EA (4.75 eV for HSO_4; Wang et al., 2000).

The $CHO/CHON \cdot (HSO_4^-/NO_3^-)$ ion group, with an overall molecular formula of $C_{2-15}H_{2-26}O_{2-13}N_{0-2} \cdot NO_3^-/HSO_4^-$, constituted a significant fraction of negative ions (31 %) at CHC. These organic ions are formed through the adduction between primary charge carriers, such as HSO_4^- and NO_3^-, and neutral OOM. These OOM are likely the oxidation products of the volatile organic compounds (VOC) from the Amazon and the adjacent La Paz – El Alto metropolitan area. While the diurnal variation was relatively small (34 % for the nighttime and 27 % for the daytime), the ion composition of $CHO/CHON \cdot (HSO_4^-/NO_3^-)$ could be significantly different between daytime and nighttime due to the availability of the charging ions (see more discussions in Section 3.2.2). A previous study from a boreal forest shows that organic ions are mainly

345   composed of CHO/CHON·NO_3^- during nighttime, and that the fraction of

346   CHO/CHON·HSO_4^- increases with the HSO_4^- signal during daytime (Bianchi et al.,

347   2017). This is also shown by the slightly positive correlation between the

348   CHO/CHON·HSO_4^- signal fraction and the total neutral OOM concentration during

349   daytime (R: 0.25; see Fig. S3b), whereas no clear dependence was found between

350   CHO/CHON·(HSO_4^-/NO_3^-) and the total neutral OOM concentration.

351   The SO_5^- ion group, consisting of SO_5^- ions and/or O_2·SO_3^- cluster ions (Bork et al.,

352   2013; Frege et al., 2017), exhibited a lower fraction (<5 %) than the aforementioned

353   ion groups during the study period. Similar to that of the $(HNO_3)_{0-1}$·NO_3^- ion group, no

354   diurnal pattern was evident for the SO_5^- ion group. This may be the result of its different

355   major formation pathways during daytime and nighttime (Bork et al., 2013; Frege et al.,

356   2017). Daytime production of SO_5^- ions is likely associated with photo-oxidation of

357   SO_2 (similar to the formation pathway of H_2SO_4; Ehn et al., 2010; Schobesberger et al.,

358   2015). This is shown in the positive correlation (R: 0.46 for daytime data in Fig. S3c)

359   between the neutral H_2SO_4 concentration and the signal fraction of the SO_5^- ion group.

360   During nighttime, however, the SO_5^- ion group is mainly composed of O_2·SO_3^- cluster

361   ions, which are possibly formed via the oxidation of SO_2 with O_3^- (producing SO_3^-),

362   and subsequent addition of O_2 (Bork et al., 2013).

363   **3.2.2 Seasonalities of negative ions**

364   For better seasonality comparison at high-altitude CHC, we calculated the average mass

365   spectra of the negative ion groups for each season (Fig. 5 for daytime and Fig. S4 for

366   nighttime). Distinct seasonalities (wet season, wet-to-dry transition period, and dry

367   season) were found for the majority of the negative ion groups at CHC, including

368    $(H_2SO_4)_{0-3}$·HSO_4^-, $(NH_3)_{1-6}$·$(H_2SO_4)_{3-7}$·HSO_4^-, SO_5^-, and organic cluster ions, as shown

369   in the averaged daytime mass spectra (Fig. 5; more detailed reason will be discussed

370   below). However, the signals of some other negative ion groups, e.g., MA-derived ions

371   and $(HNO_3)_{0-2}$·NO_3^-, were generally stable (with differences ≤ 20 %) across the seasons.

372   Such unclear seasonalities can be attributed to the high EA (Ferguson and Arnold, 1981;

373   Ravi Kumar et al., 2005) and/or the stability of the parent neutral species (Martin et al.,

374   2007; Kerminen et al., 2000; Bikkina et al., 2021). Similar patterns can also be found

375   in the average nighttime mass spectra among the seasons (Fig. S4).

376    $(H_2SO_4)_{0-3}$·HSO_4^- group exhibited much higher contribution in dry season (May) than

377   in wet season (January) and wet-to-dry transition period (April). The daytime fraction

378   of $(H_2SO_4)_{0-3}$·HSO_4^- increased continuously from 16 % in wet, 20 % in wet-to-dry

379   transition period, to 30 % in dry season. The maximum number of H_2SO_4 molecules

380   increased concurrently from 2 to 4 in the cluster ions (i.e., from $(H_2SO_4)_2$·HSO_4^- to

381    $(H_2SO_4)_4$·HSO_4^-). Similar trends were also found for other H_2SO_4-related ions, such as

382   the $(NH_3)_{1-6}$·$(H_2SO_4)_{3-7}$·HSO_4^- and SO_5^- during daytime (Fig. 5).

383
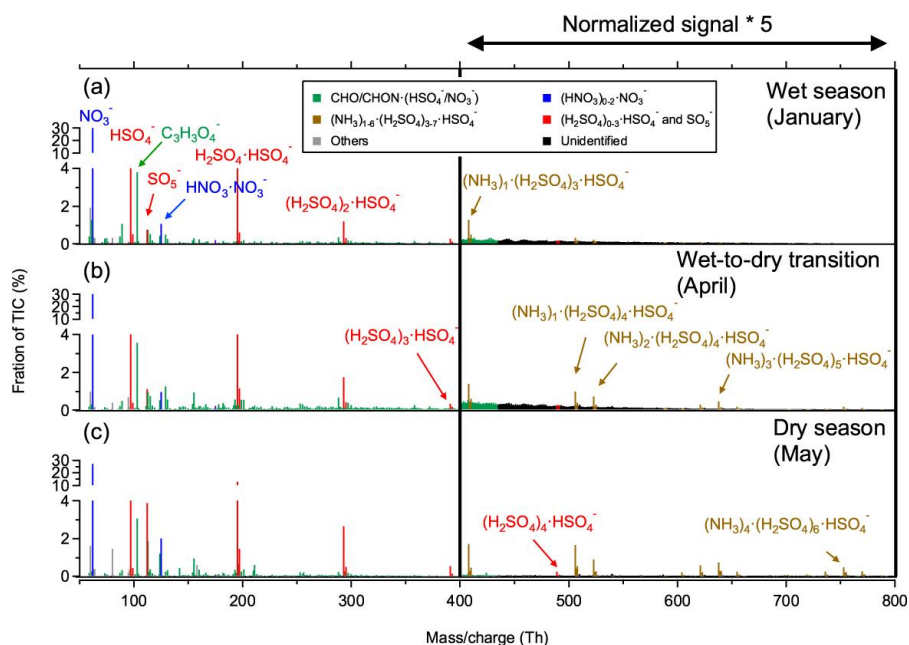
Figure 5 Mass spectra of negative ions at CHC averaged between 07:00 – 19:00 in **(a)** wet season
(January), **(b)** wet-to-dry transition period (April), and **(c)** dry season (May). The normalized signal
intensities from 400 Th to 800 Th are multiplied by a factor of 5 for better visualization.

The seasonal variations of the aforementioned H_2SO_4-related ion groups are likely due
to the changes in neutral H_2SO_4 (Fig. S5) linked to the changing synoptic-scale wind
patterns carrying different air masses with varying SO_2 (Bianchi et al., 2022). The air
mass pathways 07_PW and 08_PW, covering the Western and Northern Altiplano
plateau (see Table 1 and Fig. 2a), where active volcanic degassing of SO_2 has been
reported (Moussallam et al., 2017; Carn et al., 2017), had their largest influence on
CHC in dry season (i.e., May; see Fig. 2). The corresponding daytime fractions of
$(H_2SO_4)_{0-3} \cdot HSO_4^-$ from these two pathways (Fig. 6a) were also the highest (27 % and
32 %, respectively). In contrast, air mass pathways 03_PW and 12_PW, originating in
the Amazon Basin and Eastern/South-Eastern Lowlands, exerted their most significant
impact on CHC in wet season (i.e., January) with lower daytime fractions of $(H_2SO_4)_{0-3} \cdot HSO_4^-$ (13 % and 14 %, respectively). The low fractions of H_2SO_4-related cluster ions
in wet season are also consistent with the lower SO_2 level in the Amazon Basin
compared to the Altiplano plateau (Andreae et al., 1990). As for the wet-to-dry
transition period (i.e., April), 05_PW covering both the South-Eastern Lowlands and
Southern Altiplano plateau (where volcanic degassing is also significant; Carn et al.,
2017) had an evident influence on CHC, resulting in a substantial level of H_2SO_4-related cluster ions (21 % for daytime). It is also noted that, because of the much lower
nocturnal neutral H_2SO_4 concentrations, the nighttime fractions of H_2SO_4-related
cluster ions in all air mass pathways (Fig. 7b) were generally low (< 3 %) and no clear

14

407   seasonality was found.

408   The organic cluster ion group exhibited a distinct seasonal variation than the $(H_2SO_4)_{0-}$
409    $_3 \cdot HSO_4^-$. The signal fraction of organic cluster ions was higher in wet season (31 % for
410   daytime and 32 % for nighttime) than in dry season (23 % for daytime and 27 % for
411   nighttime; Fig. 5 and Fig. S4), but it was highest for the wet-to-dry transition period
412   (46 % for daytime and 52 % for nighttime; see Fig. 6).

413   The seasonal changes of organic cluster ions could be due to the combined effect of
414   different meteorological conditions and VOC from different air mass origins (see Fig.
415   2). The air masses that originated from the Amazon Basin and Lowlands (03_PW and
416   12_PW) showed their largest impact on CHC in wet season (i.e., January). They
417   contained higher fractions of organic cluster ions, which were 35 % and 34 % for
418   daytime, and 50 % and 45 % for nighttime, respectively (Fig. 6). In dry season (i.e.,
419   May), however, the changes in air mass origin towards the Altiplano plateau and the
420   Pacific Ocean led to a lower content of organic cluster ions. The organic cluster ion
421   fractions for 07_PW and 08_PW (largest influence on CHC in dry season) in May were
422   23 % and 19 % for daytime, and 29 % and 27 % for nighttime, respectively. As for the
423   wet-to-dry transition period (i.e., April), due to the combined influences of biogenic
424   and anthropogenic VOC sources from 05_PW (evident impact on CHC in April),
425   covering the South-Eastern Lowlands and the Southern Altiplano plateau, the
426   corresponding organic cluster ion fractions from this air mass pathway were also the
427   highest (41 % for daytime and 53 % for nighttime; see Fig. 6).
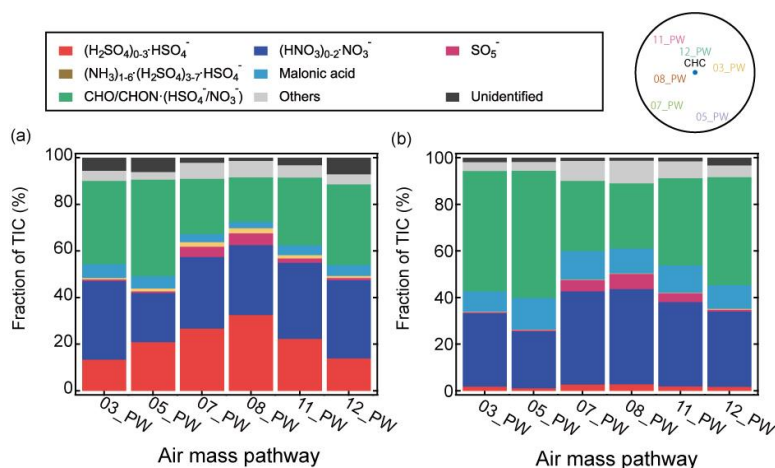

428

429   Figure 6 The fractions of the negative ion groups observed at CHC determined during the representative
430   periods of each air mass pathway (described in Section 2.3.2) for **(a)** daytime (07:00 – 19:00) and **(b)**
431   nighttime (19:00 – 07:00). A sketch of the horizontal profile of the air mass pathways (Fig. 2a) is shown
432   in the upper right corner for clarity.

433 A further investigation of the organic ion group shows that the seasonal trends of the
434 individual organic ions also varied (Fig. 7 for daytime and Fig. S6 for nighttime).
435 Whereas the majority of the organic cluster ions at CHC were more abundant during
436 wet season (Fig. 7a and Fig. S6a), fractions of CHO/CHON·HSO_4^- increased during the
437 dry season. The observed increases of CHO/CHON·HSO_4^- cluster ions could be
438 associated with the increased HSO_4^-/NO_3^- ratios in dry season (Fig. 5 and Fig. S4).
439 Similar increases of CHO/CHON·HSO_4^- cluster ions were also found to relate to the
440 ratio of HSO_4^-/NO_3^- in a boreal forest environment (Bianchi et al., 2017). In addition,
441 changes in OOM composition between wet and dry seasons may also play a role (Fig.
442 7b and Fig. S6b), as NO_3^- tends to cluster with OOM containing hydroxyl and
443 hydroperoxyl functional groups (Hyttinen et al., 2015) while some other observed
444 OOM may be more efficiently charged by HSO_4^-.

445 The seasonal variations of the individual organic cluster ions are likely caused by
446 different air masses (Fig. 7b and Fig. S6b). The air masses influenced by tropical
447 rainforest vegetation from the Amazon Basin are dominated by isoprene (C_5H_8)
448 emissions and isoprene oxidation products (Bianchi et al., 2022). This region
449 corresponds to 03_PW and 12_PW (largest impact on CHC in wet season in January)
450 consisting of relatively higher fractions of organic cluster ions with OOM containing
451 4-5 carbon atoms (50 % and 46 % for nighttime, and 29 % and 32 % for daytime,
452 respectively). In contrast, when the air masses were more influenced by the Altiplano
453 plateau (i.e., 05_PW, 07_PW, and 08_PW, with more anthropogenic emissions and less
454 vegetation) in wet-to-dry transition period and dry season, organic cluster ions with 6-
455 8 carbon atoms, potentially originating from anthropogenic sources (e.g., toluene
456 (C_7H_8); Huang et al., 2019; Cai et al., 2022), were of higher contributions. The signal
457 fractions of these organic ions were thus the highest in these air mass pathways,
458 accounting for 36-39 % for nighttime and 37-39 % for daytime. For all the air mass
459 pathways, fractions of organic ions with more than 9 carbon atoms were relatively low
460 (<10 %). This might be due to their lower volatilities compared to OOM with smaller
461 carbon numbers (Donahue et al., 2012), resulting in a larger probability of them being
462 removed during their transport to CHC (e.g., condensing on pre-existing particles).
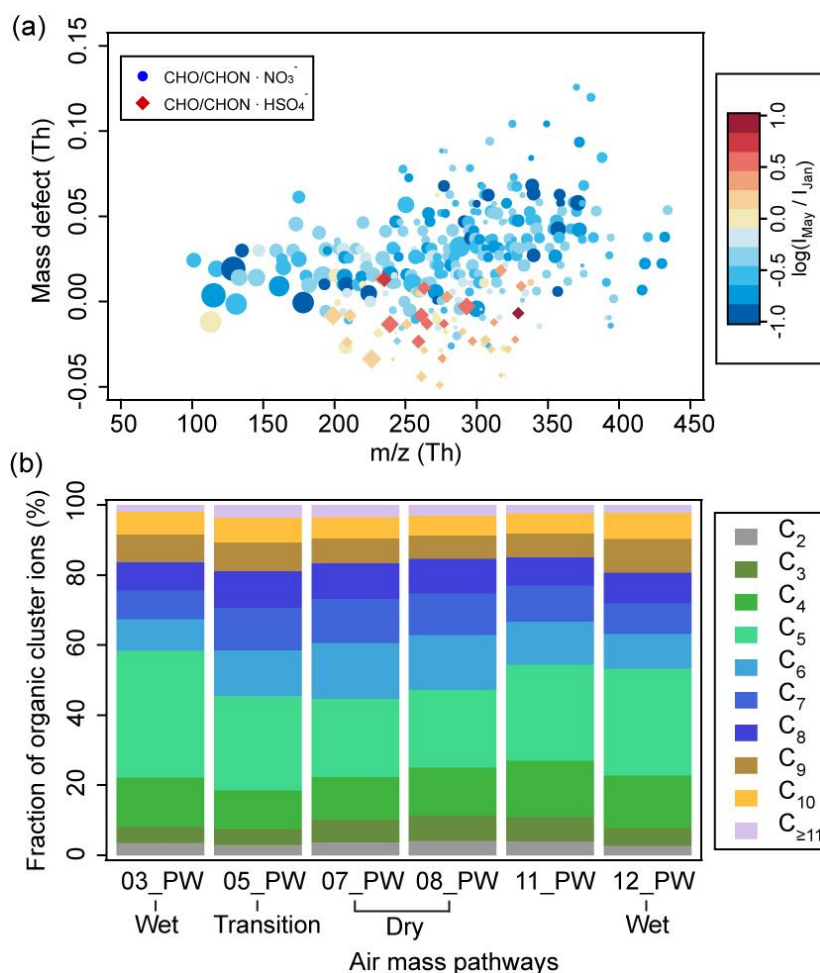
463

464 Figure 7 (**a**) Mass defect plot of organic cluster ions during nighttime (19:00-07:00). The color code
465 indicates ratios (in log scale) between median signals of each ion detected in May (I_{May}) of dry season
466 and January (I_{Jan}) of wet season. The marker size is proportional to the log-transformed median signals
467 of ions in May. (**b**) Fraction of organic cluster ions from different air mass pathways as a function of
468 carbon atom numbers during nighttime (19:00-07:00). A similar figure based on daytime data (07:00-
469 19:00) is in the supplementary information (Figure S5). Note that MA-derived ions were not included in
470 this figure.

471 **3.3 Positive ions**

472 Several positive cluster ion groups were consistently observed in February and March
473 (i.e., wet season) during the study period. Based on their chemical composition, the
474 positive cluster ions measured at CHC are classified into four groups (Fig. 8): (1) a
475 series of protonated amines, including trimethylamine ($C_3H_9N \cdot H^+$), pyridine
476 ($C_5H_7N \cdot H^+$), aniline ($C_6H_7N \cdot H^+$), and benzylamine ($C_7H_9 N \cdot H^+$); (2) organic cluster

477 ions consisting of OOM (identified as $C_{3-24}H_{6-39}O_{2-12}N_{0-2}$) clustered with positive
478 charge carriers such as protons (H^+), ammonium (NH_4^+), and aminium (NH^+) ions; (3)
479 contamination ions; and (4) unidentified ions (likely organic ions in higher masses;
480 Bianchi et al., 2021). Contamination in the positive cluster ions includes
481 ethylhexylglycerin (e.g., $C_{11}H_{24}O_3 \cdot NH^+$), which is widely used in cosmetics (Aerts et
482 al., 2016), and polydimethylsiloxane (e.g., $(C_2H_6OSi)_7 \cdot NH_4^+$) possibly from instrument
483 tubing (Bianchi et al., 2014). In contrast to the negative cluster ions, the four positive
484 cluster ion groups were generally stable with smaller diurnal variability over the study
485 period (Fig. 9). This is similar to the diurnal patterns determined in previous studies in
486 a boreal forest environment (Ehn et al., 2010) and at the JFJ (Frege et al., 2017).
487 However, due to the unavailable measurements of the corresponding neutral species
488 (e.g., amines), the exact reason for such weak diurnal variations observed in different
489 locations remains unclear.
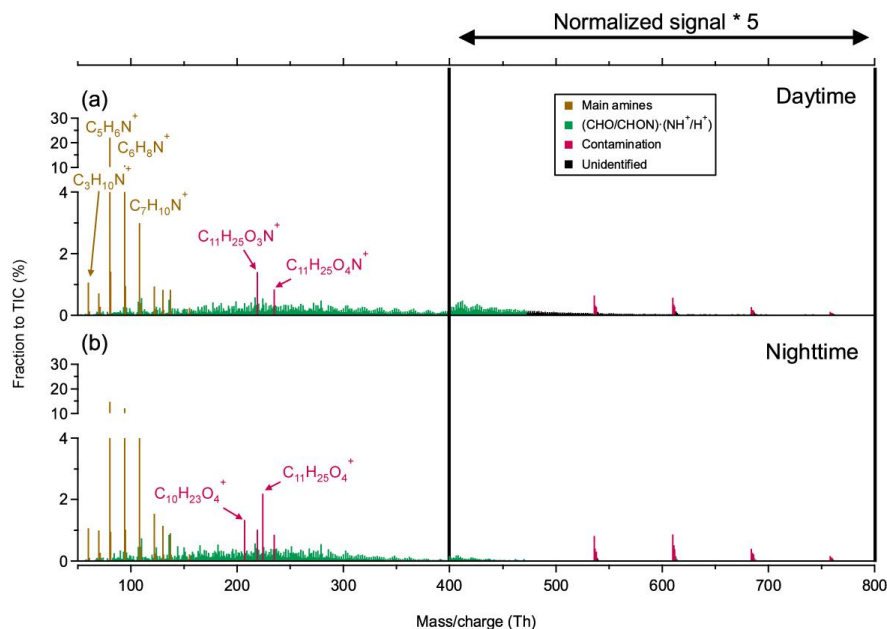
491 Figure 8 Averaged mass spectra of positive ions at CHC in February and March 2018 when APi-TOF
492 was operating in positive ion mode (see section 2.2.1), during **(a)** daytime (07:00 – 19:00) and **(b)**
493 nighttime (19:00 – 07:00). The normalized signal intensities from 400 Th to 800 Th are multiplied by a
494 factor of 5 for better visualization.

495 The protonated amines were the most abundant positive ion group (46 %), with no
496 significant diurnal variations. Nighttime contributions of this ion group (47 %) were
497 similar to its daytime contributions (45 %; Fig. 9). They also dominated the positive
498 ion spectra observed in different environments, such as a boreal forest (Ehn et al., 2010),
499 the JFJ (Frege et al., 2017), and the free troposphere (Schulte and Arnold, 1990). Their

500 sources have not been fully identified (Kosyakov et al., 2020), but they are widely used
501 as solvents and dyes (Sims et al., 1989), which may be potential sources of these ions
502 observed at CHC.
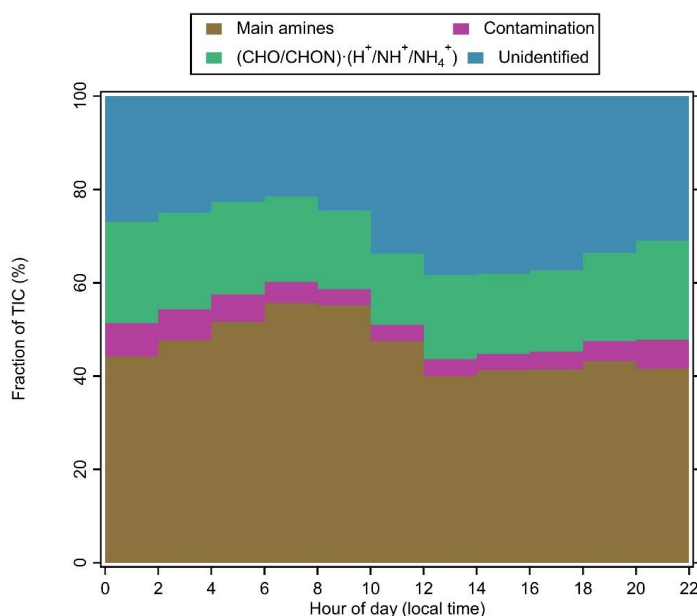
503
504 Figure 9 Diurnal variation of positive ion groups at CHC, averaged over measurements in February and
505 March 2018 (when APi-TOF was operating in positive ion mode, see section 2.2.1).

506 Positive organic cluster ions were also relatively abundant (19 %) at CHC during the
507 wet season. Similar to the negative organic ions in wet season (Fig. 6), this reflects the
508 influence of air masses originating from the Amazon Basin and Eastern/South-Eastern
509 Lowlands (e.g., 03_PW and 11_PW). Differences in the positive organic ion signals
510 between nighttime (21 %) and daytime (18 %) were small, which is similar to the
511 negative organic cluster ions (see Fig. 3). A further investigation of the relationship
512 between these positive ions and their neutral species is, unfortunately, not possible due
513 to the unavailability of CI-APi-TOF data in February and March caused by instrumental
514 issues.

515 **3.4 Potential connections between atmospheric ions and new particle**
516 **formation events**

517 During the SALTENA campaign from January to May 2018, NPF events were
518 frequently observed at CHC (Fig. S7). While most of them occurred from April (the
519 wet-to-dry transition period, 21 events) to May (dry season, 26 events), NPF events
520 seldom occurred during wet season from January to March (8 events in total).
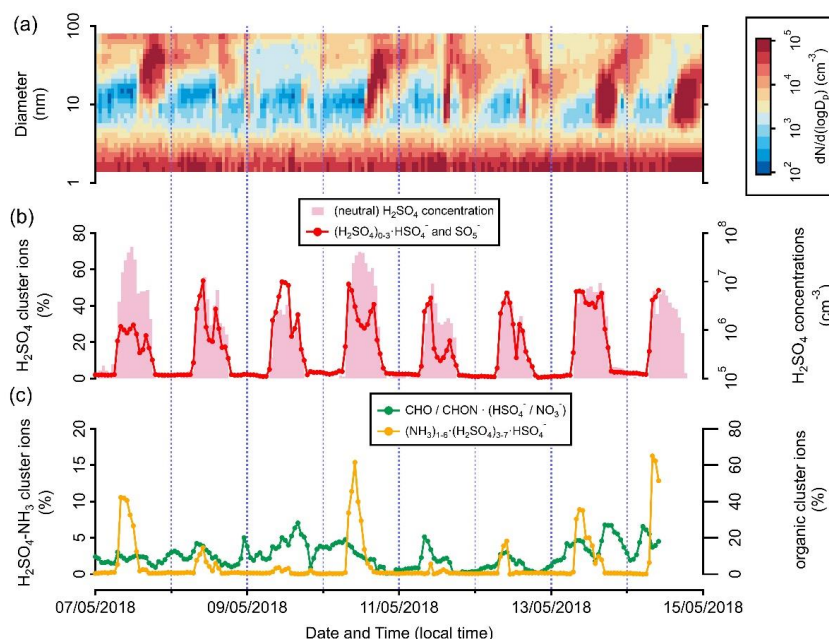
521

522   Figure 10 Time series of the **(a)** size distribution of aerosol particles (measured with NAIS and MPSS),
523   **(b)** signal fraction of the $(H_2SO_4)_{0-3}\cdot HSO_4^-$ ion group and neutral H_2SO_4 concentration, and **(c)** signal
524   fractions of the $(NH_3)_{1-6}\cdot (H_2SO_4)_{3-7}\cdot HSO_4^-$ and negative organic cluster ion groups, observed at CHC
525   from 7 to 14 May 2018 when NPF occurred frequently.

526   Previous field studies at high-altitude mountain sites have shown that NPF events can
527   be triggered by different compounds, such as low-volatile neutral OOM (Bianchi et al.,
528   2021), neutral H_2SO_4 and OOM (Bianchi et al., 2016), and H_2SO_4-NH_3 cluster ions
529   (Frege et al., 2017). While the signal fractions of the negative organic cluster ions did
530   not seem to have a strong correlation with the onset of the NPF events, the fractions of
531   the $(NH_3)_{1-6}\cdot (H_2SO_4)_{3-7}\cdot HSO_4^-$ (associated with $(H_2SO_4)_{0-3}\cdot HSO_4^-$) always peaked
532   before NPF events, and started to decrease when NPF started (see example NPF events
533   on, e.g., 7, 10, 13, and 14 May 2018; Fig. 10).

534   Moreover, higher levels (up to an order of magnitude) of $(NH_3)_{1-6}\cdot (H_2SO_4)_{3-7}\cdot HSO_4^-$
535   and $(H_2SO_4)_{0-3}\cdot HSO_4^-$ ions as well as negative organic cluster ions charged by HSO_4^-
536   were also observed during the NPF days (Fig. 11). In contrast, other negative ion groups
537   (e.g., the majority of the negative organic cluster ions charged by NO_3^-) were more
538   abundant during the non-NPF days. Our observations indicate a potentially important
539   role of $(NH_3)_{1-6}\cdot (H_2SO_4)_{3-7}\cdot HSO_4^-$ cluster ions in NPF events at CHC from January to
540   May 2018, particularly in wet-to-dry transition period and dry season.

541
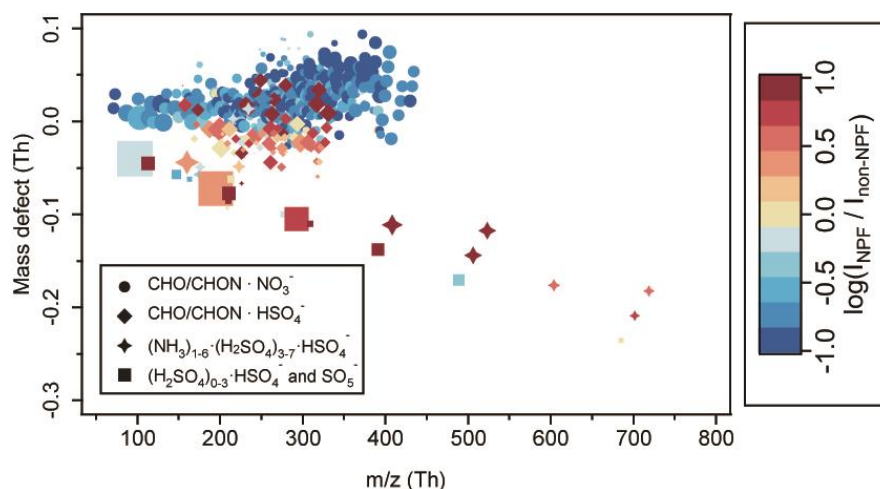
Figure 11 Mass defect plot of differences in negative cluster ion composition between NPF and non-NPF
days. The negative ion composition of NPF events was averaged over all NPF days from 08:00 to 12:00
in January, April, and May 2018 (when APi-TOF was operating in negative ion mode, see section 2.2.1)
at CHC. The ion composition of non-NPF days was averaged over non-NPF days from 08:00 to 12:00
for the same period. The x-axis is the exact mass of cluster ions, and the y-axis is the mass defect. The
color code indicates ratios (in log scale) between median signals of each ion determined in NPF events
(I_{NPF}) and non-NPF periods ($I_{non\text{-}NPF}$). The marker size is proportional to the log-transformed median
signals of ions observed in the NPF events that occurred in January, April and May. Note that $(HNO_3)_{0-2} \cdot NO_3^-$ cluster ions were not included here.

The majority of the observed NPF events occurred when CHC was more impacted by
air masses originating from source regions with elevated SO_2 emissions (05_PW,
07_PW, and 08_PW). This is similar to the observations from the high-altitude station
JFJ (Frege et al., 2017). In addition, the fraction of large positive organic cluster ions
(mass range from 500 to 800 Th; Fig. S8) was found to increase during the NPF events
in the wet season. Such large positive organic ions have been found to contribute to
NPF in the Himalayas (Bianchi et al., 2021), and thus, their contribution to NPF can
not be completely ruled out at CHC as well.

4. Conclusion

In this study, both negative and positive atmospheric ions were measured at a high-
altitude research station (CHC) in the Bolivian Andes for five months, from January to
May 2018, using an APi-TOF mass spectrometer. Negative ions were mainly composed
of $(H_2SO_4)_{0-3} \cdot HSO_4^-$, $(HNO_3)_{0-2} \cdot NO_3^-$, SO_5^-, $(NH_3)_{1-6} \cdot (H_2SO_4)_{3-7} \cdot HSO_4^-$, MA-derived,
and $CHO/CHON \cdot (HSO_4^-/NO_3^-)$ ion groups. Positive ions mainly consisted of a series
of protonated amines $(C_{3-7}H_{7-9}N \cdot H^+)$ and organic cluster ions
$CHO/CHON \cdot (H^+/NH_4^+/NH^+)$. Distinct diurnal variation was observed for the negative
ions, and attributed mainly to the changes in the corresponding neutral species'

568   concentrations and/or their EA / PA. An example is H_2SO_4-related cluster ions, the diel
569   temporal variation of which was mainly due to the photochemical production of neutral
570   H_2SO_4 during daytime. Strong seasonality of negative ions was also found, such as for
571   H_2SO_4-related cluster ions owing to changes in SO_2 and the resulting neutral H_2SO_4
572   concentrations. The seasonal variation was mainly because of the differences in source
573   regions of air masses arriving at CHC from wet to dry seasons. In contrast, no
574   significant diurnal variation was observed for the positive ions. The comparison
575   between NPF and non-NPF days infers that H_2SO_4-NH_3 cluster ions contribute to the
576   aerosol nucleation process at CHC, particularly in wet-to-dry transition period and dry
577   season when CHC was more impacted by air masses originating from source regions
578   with elevated SO_2 emissions. The results further indicate that atmospheric ion
579   composition at CHC is directly affected by air masses from different source regions.

580   Measurements of atmospheric ions in the field will improve understanding of
581   atmospheric physical and chemical processes in the study regions, as the ions play
582   important roles in atmospheric chemistry through participation in or catalysis of ion-
583   molecule reactions and ion-induced new particle formation. Our study thus provides
584   new insights into the chemical composition of atmospheric ions and their potential role
585   in high-altitude NPF in the Bolivian Andes where both natural (e.g., biogenic and
586   volcanic) and anthropogenic emissions are important.
587

610

611 **Reference**

612 Aerts, O., Verhulst, L., and Goossens, A.: Ethylhexylglycerin: a low-risk, but highly
613 relevant, sensitizer in 'hypo-allergenic' cosmetics, Contact Dermatitis, 74, 281–288,
614 https://doi.org/10/f8h4cb, 2016.

615 Aliaga, D., Sinclair, V. A., Andrade, M., Artaxo, P., Carbone, S., Kadantsev, E., Laj, P.,
616 Wiedensohler, A., Krejci, R., and Bianchi, F.: Identifying source regions of air masses
617 sampled at the tropical high-altitude site of Chacaltaya using WRF-FLEXPART and
618 cluster analysis, Atmos. Chem. Phys., 21, 16453–16477, https://doi.org/10/gnhzvm,
619 2021.

620 Andrade, M., Zaratti, F., Forno, R., Gutiérrez, R., Moreno, I., Velarde, F., Ávila, F.,
621 Roca, M., Sánchez, M., Laj, P., Jaffrezo, J., Ginot, P., Sellegri, K., Ramonet, M., Laurent,
622 O., Weinhold, K., Wiedensohler, A., Krejci, R., Bonasoni, P., Cristofanelli, P.,
623 Whiteman, D., Vimeux, F., Dommergue, A., and Magand, O.: Puesta en marcha de una
624 nueva estación de monitoreo climático en los andes centrales de Bolivia: la estación
625 Gaw/Chacaltaya, Rev. Boliv. Física, 26, 06–15, 2015.

626 Andreae, M. O., Berresheim, H., Bingemer, H., Jacob, D. J., Lewis, B. L., Li, S.-M.,
627 and Talbot, R. W.: The atmospheric sulfur cycle over the Amazon Basin: 2. Wet season,
628 J. Geophys. Res., 95, 16813, https://doi.org/10.1029/JD095iD10p16813, 1990.

629 Beck, L. J., Sarnela, N., Junninen, H., Hoppe, C. J. M., Garmash, O., Bianchi, F., Riva,
630 M., Rose, C., Peräkylä, O., Wimmer, D., Kausiala, O., Jokinen, T., Ahonen, L., Mikkilä,
631 J., Hakala, J., He, X.-C., Kontkanen, J., Wolf, K. K. E., Cappelletti, D., Mazzola, M.,
632 Traversi, R., Petroselli, C., Viola, A. P., Vitale, V., Lange, R., Massling, A., Nøjgaard, J.
633 K., Krejci, R., Karlsson, L., Zieger, P., Jang, S., Lee, K., Vakkari, V., Lampilahti, J.,
634 Thakur, R. C., Leino, K., Kangasluoma, J., Duplissy, E.-M., Siivola, E., Marbouti, M.,
635 Tham, Y. J., Saiz-Lopez, A., Petäjä, T., Ehn, M., Worsnop, D. R., Skov, H., Kulmala,
636 M., Kerminen, V.-M., and Sipilä, M.: Differing Mechanisms of New Particle Formation
637 at   Two   Arctic   Sites,   Geophys.   Res.   Lett.,   48,   e2020GL091334,
638 https://doi.org/10.1029/2020GL091334, 2021.

639 Bianchi, F., Praplan, A. P., Sarnela, N., Dommen, J., Kürten, A., Ortega, I. K.,
640 Schobesberger, S., Junninen, H., Simon, M., Tröstl, J., Jokinen, T., Sipilä, M., Adamov,
641 A., Amorim, A., Almeida, J., Breitenlechner, M., Duplissy, J., Ehrhart, S., Flagan, R.
642 C., Franchin, A., Hakala, J., Hansel, A., Heinritzi, M., Kangasluoma, J., Keskinen, H.,
643 Kim, J., Kirkby, J., Laaksonen, A., Lawler, M. J., Lehtipalo, K., Leiminger, M.,
644 Makhmutov, V., Mathot, S., Onnela, A., Petäjä, T., Riccobono, F., Rissanen, M. P.,
645 Rondo, L., Tomé, A., Virtanen, A., Viisanen, Y., Williamson, C., Wimmer, D., Winkler,
646 P. M., Ye, P., Curtius, J., Kulmala, M., Worsnop, D. R., Donahue, N. M., and
647 Baltensperger, U.: Insight into acid-base nucleation experiments by comparison of the
648 chemical composition of positive, negative, and neutral clusters, Environ. Sci. Technol.,
649 48, 13675–13684, https://doi.org/10.1021/es502380b, 2014.

650   Bianchi, F., Tröstl, J., Junninen, H., Frege, C., Henne, S., Hoyle, C. R., Molteni, U.,
651   Herrmann, E., Adamov, A., Bukowiecki, N., Chen, X., Duplissy, J., Gysel, M., Hutterli,
652   M., Kangasluoma, J., Kontkanen, J., Kürten, A., Manninen, H. E., Münch, S., Peräkylä,
653   O., Petäjä, T., Rondo, L., Williamson, C., Weingartner, E., Curtius, J., Worsnop, D. R.,
654   Kulmala, M., Dommen, J., and Baltensperger, U.: New particle formation in the free
655   troposphere: A question of chemistry and timing., Science, 352, 1109–12,
656   https://doi.org/10.1126/science.aad5456, 2016.

657   Bianchi, F., Garmash, O., He, X., Yan, C., Iyer, S., Rosendahl, I., Xu, Z., Rissanen, M.
658   P., Riva, M., Taipale, R., Sarnela, N., Petäjä, T., Worsnop, D. R., Kulmala, M., Ehn, M.,
659   and Junninen, H.: The role of highly oxygenated molecules (HOMs) in determining the
660   composition of ambient ions in the boreal forest, Atmos. Chem. Phys., 17, 13819–
661   13831, https://doi.org/10.5194/acp-17-13819-2017, 2017.

662   Bianchi, F., Junninen, H., Bigi, A., Sinclair, V. A., Dada, L., Hoyle, C. R., Zha, Q., Yao,
663   L., Ahonen, L. R., Bonasoni, P., Buenrostro Mazon, S., Hutterli, M., Laj, P., Lehtipalo,
664   K., Kangasluoma, J., Kerminen, V. M., Kontkanen, J., Marinoni, A., Mirme, S., Molteni,
665   U., Petäjä, T., Riva, M., Rose, C., Sellegri, K., Yan, C., Worsnop, D. R., Kulmala, M.,
666   Baltensperger, U., and Dommen, J.: Biogenic particles formed in the Himalaya as an
667   important source of free tropospheric aerosols, Nat. Geosci., 14, 4–9,
668   https://doi.org/10.1038/s41561-020-00661-5, 2021.

669   Bianchi, F., Sinclair, V. A., Aliaga, D., Zha, Q., Scholz, W., Wu, C., Heikkinen, L.,
670   Modini, R., Partoll, E., Velarde, F., Moreno, I., Gramlich, Y., Huang, W., Leiminger, M.,
671   Enroth, J., Peräkylä, O., Marinoni, A., Xuemeng, C., Blacutt, L., Forno, R., Gutierrez,
672   R., Ginot, P., Uzu, G., Facchini, M. C., Gilardoni, S., Gysel-Beer, M., Cai, R., Petäjä,
673   T., Rinaldi, M., Saathoff, H., Sellegri, K., Worsnop, D., Artaxo, P., Hansel, A., Kulmala,
674   M., Wiedensohler, A., Laj, P., Krejci, R., Carbone, S., Andrade, M., and Mohr, C.: The
675   SALTENA experiment: Comprehensive observations of aerosol sources, formation and
676   processes in the South American Andes, Bull. Am. Meteorol. Soc., 1, 1–46,
677   https://doi.org/10.1175/BAMS-D-20-0187.1, 2022.

678   Bikkina, S., Kawamura, K., Sakamoto, Y., and Hirokawa, J.: Low molecular weight
679   dicarboxylic acids, oxocarboxylic acids and α-dicarbonyls as ozonolysis products of
680   isoprene: Implication for the gaseous-phase formation of secondary organic aerosols,
681   Sci. Total Environ., 769, 144472, https://doi.org/10.1016/j.scitotenv.2020.144472,
682   2021.

683   Bork, N., Kurtén, T., and Vehkamäki, H.: Exploring the atmospheric chemistry of
684   $O_2SO_3^-$ and assessing the maximum turnover number of ion-catalysed H_2SO_4 formation,
685   Atmos. Chem. Phys., 13, 3695–3703, https://doi.org/10.5194/acp-13-3695-2013, 2013.

686   Boulon, J., Sellegri, K., Venzac, H., Picard, D., Weingartner, E., Wehrle, G., Collaud
687   Coen, M., Bütikofer, R., Flückiger, E., Baltensperger, U., and Laj, P.: New particle
688   formation and ultrafine charged aerosol climatology at a high altitude site in the Alps

689   (Jungfraujoch, 3580 m a.s.l., Switzerland), Atmos. Chem. Phys., 10, 9333–9349,
690   https://doi.org/10.5194/ACP-10-9333-2010, 2010.

691   Brioude, J., Arnold, D., Stohl, A., Cassiani, M., Morton, D., Seibert, P., Angevine, W.,
692   Evan, S., Dingwell, A., Fast, J. D., Easter, R. C., Pisso, I., Burkhart, J., and Wotawa, G.:
693   The Lagrangian particle dispersion model FLEXPART-WRF version 3.1, Geosci.
694   Model Dev., 6, 1889–1904, https://doi.org/10.5194/gmd-6-1889-2013, 2013.

695   Cai, J., Wu, C., Wang, J., Du, W., Zheng, F., Hakala, S., Fan, X., Chu, B., Yao, L., Feng,
696   Z., Liu, Y., Sun, Y., Zheng, J., Yan, C., Bianchi, F., Kulmala, M., Mohr, C., and
697   Daellenbach, K. R.: Influence of organic aerosol molecular composition on particle
698   absorptive properties in autumn Beijing, Atmos. Chem. Phys., 22, 1251–1269,
699   https://doi.org/10.5194/acp-22-1251-2022, 2022.

700   Carn, S. A., Fioletov, V. E., McLinden, C. A., Li, C., and Krotkov, N. A.: A decade of
701   global volcanic SO_2 emissions measured from space, Sci. Rep., 7, 44095,
702   https://doi.org/10/f9tdsj, 2017.

703   Coen, M. C., Andrews, E., Aliaga, D., Andrade, M., Angelov, H., Bukowiecki, N., Ealo,
704   M., Fialho, P., Flentje, H., Gannet Hallar, A., Hooda, R., Kalapov, I., Krejci, R., Lin,
705   N.-H. H., Marinoni, A., Ming, J., Nguyen, N. A., Pandolfi, M., Pont, V., Ries, L.,
706   Rodríguez, S., Schauer, G., Sellegri, K., Sharma, S., Sun, J., Tunved, P., Velasquez, P.,
707   Ruffieux, D., Hallar, A. G., Hooda, R., Kalapov, I., Krejci, R., Lin, N.-H. H., Marinoni,
708   A., Ming, J., Nguyen, A., Pandolfi, M., Pont, V., Ries, L., Rodríguez, S., Schauer, G.,
709   Sellegri, K., Sharma, S., Sun, J., Tunved, P., Velasquez, P., and Ruffieux, D.:
710   Identification of topographic features influencing aerosol observations at high altitude
711   stations, Atmos. Chem. Phys., 18, 12289–12313, https://doi.org/10.5194/acp-18-
712   12289-2018, 2018.

713   Donahue, N. M., Kroll, J. H., Pandis, S. N., and Robinson, A. L.: A two-dimensional
714   volatility basis set – Part 2: Diagnostics of organic-aerosol evolution, Atmos. Chem.
715   Phys., 12, 615–634, https://doi.org/10.5194/acp-12-615-2012, 2012.

716   Ehn, M., Junninen, H., Petäjä, T., Kurtén, T., Kerminen, V.-M., Schobesberger, S.,
717   Manninen, H. E., Ortega, I. K., Vehkamäki, H., Kulmala, M., and Worsnop, D. R.:
718   Composition and temporal behavior of ambient ions in the boreal forest, Atmos. Chem.
719   Phys., 10, 8513–8530, https://doi.org/10.5194/acp-10-8513-2010, 2010.

720   Eisele, F. L.: Identification of tropospheric ions, J. Geophys. Res. Atmos., 91, 7897–
721   7906, https://doi.org/10/bdscqw, 1986.

722   Ferguson, E. E. and Arnold, F.: Ion chemistry of the stratosphere, Acc. Chem. Res., 14,
723   327–334, https://doi.org/10.1021/ar00071a001, 1981.

724   Frege, C., Bianchi, F., Molteni, U., Tröstl, J., Junninen, H., Henne, S., Sipilä, M.,
725   Herrmann, E., Rossi, M. J., Kulmala, M., Hoyle, C. R., Baltensperger, U., and Dommen,
726   J.: Chemical characterization of atmospheric ions at the high altitude research station

727   Jungfraujoch   (Switzerland),   Atmos.   Chem.   Phys,   17,   2613–2629,
728   https://doi.org/10.5194/acp-17-2613-2017, 2017.

729   Hirsikko, A., Laakso, L., Hõrrak, U., Aalto, P. P., Kerminen, V., and Kulmala, M.:
730   Annual and size dependent variation of growth rates and ion concentrations in boreal
731   forest, Boreal Env, Res, 357–369, 2005.

732   Hirsikko, A., Nieminen, T., Gagné, S., Lehtipalo, K., Manninen, H. E., Ehn, M., Hõrrak,
733   U., Kerminen, V.-M., Laakso, L., Mcmurry, P. H., Mirme, A., Mirme, S., Petäjä, T.,
734   Tammet, H., Vakkari, V., Vana, M., and Kulmala, M.: Atmospheric Chemistry and
735   Physics Atmospheric ions and nucleation: a review of observations, Atmos. Chem Phys,
736   11, 767–798, https://doi.org/10.5194/acp-11-767-2011, 2011.

737   Huang, W., Saathoff, H., Shen, X., Ramisetty, R., Leisner, T., and Mohr, C.: Seasonal
738   characteristics of organic aerosol chemical composition and volatility in Stuttgart,
739   Germany, Atmos. Chem. Phys., 19, 11687–11700, https://doi.org/10.5194/acp-19-
740   11687-2019, 2019.

741   Hyttinen, N., Kupiainen-Määttä, O., Rissanen, M. P., Muuronen, M., Ehn, M., and
742   Kurtén, T.: Modeling the Charging of Highly Oxidized Cyclohexene Ozonolysis
743   Products Using Nitrate-Based Chemical Ionization, J. Phys. Chem. A, 119, 6339–6345,
744   https://doi.org/10.1021/acs.jpca.5b01818, 2015.

745   Jokinen, T., Sipilä, M., Junninen, H., Ehn, M., Lönn, G., Hakala, J., Petäjä, T., Mauldin,
746   R. L., Kulmala, M., and Worsnop, D. R.: Atmospheric sulphuric acid and neutral cluster
747   measurements   using   CI-APi-TOF,   Atmos.   Chem.   Phys.,   12,   4117–4125,
748   https://doi.org/10.5194/acp-12-4117-2012, 2012.

749   Jokinen, T., Sipilä, M., Kontkanen, J., Vakkari, V., Tisler, P., Duplissy, E.-M., Junninen,
750   H., Kangasluoma, J., Manninen, H. E., Petäjä, T., Kulmala, M., Worsnop, D. R., Kirkby,
751   J., Virkkula, A., and Kerminen, V.-M.: Ion-induced sulfuric acid–ammonia nucleation
752   drives   particle   formation   in   coastal   Antarctica,   Sci.   Adv.,   4,   eaat9744,
753   https://doi.org/10.1126/sciadv.aat9744, 2018.

754   Junninen, H., Ehn, M., Petäjä, T., Luosujärvi, L., Kotiaho, T., Kostiainen, R., Rohner,
755   U., Gonin, M., Fuhrer, K., Kulmala, M., and Worsnop, D. R.: A high-resolution mass
756   spectrometer to measure atmospheric ion composition, Atmos. Meas. Tech., 3, 1039–
757   1053, https://doi.org/10.5194/amt-3-1039-2010, 2010.

758   Kerminen, V.-M., Ojanen, C., Pakkanen, T., Hillamo, R., Aurela, M., and Meriläinen,
759   J.: Low-molecular-weight dicarboxylic acids in an urban and rural atmosphere, J.
760   Aerosol Sci., 31, 349–362, https://doi.org/10.1016/S0021-8502(99)00063-4, 2000.

761   Kirkby, J., Curtius, J., Almeida, J., Dunne, E., Duplissy, J., Ehrhart, S., Franchin, A.,
762   Gagné, S., Ickes, L., Kürten, A., Kupc, A., Metzger, A., Riccobono, F., Rondo, L.,
763   Schobesberger, S., Tsagkogeorgas, G., Wimmer, D., Amorim, A., Bianchi, F.,
764   Breitenlechner, M., David, A., Dommen, J., Downard, A., Ehn, M., Flagan, R. C.,

765   Haider, S., Hansel, A., Hauser, D., Jud, W., Junninen, H., Kreissl, F., Kvashin, A.,
766   Laaksonen, A., Lehtipalo, K., Lima, J., Lovejoy, E. R., Makhmutov, V., Mathot, S.,
767   Mikkilä, J., Minginette, P., Mogo, S., Nieminen, T., Onnela, A., Pereira, P., Petäjä, T.,
768   Schnitzhofer, R., Seinfeld, J. H., Sipilä, M., Stozhkov, Y., Stratmann, F., Tomé, A.,
769   Vanhanen, J., Viisanen, Y., Vrtala, A., Wagner, P. E., Walther, H., Weingartner, E., Wex,
770   H., Winkler, P. M., Carslaw, K. S., Worsnop, D. R., Baltensperger, U., and Kulmala, M.:
771   Role of sulphuric acid, ammonia and galactic cosmic rays in atmospheric aerosol
772   nucleation, Nature, 476, 429–433, https://doi.org/10.1038/nature10343, 2011.

773   Kirkby, J., Duplissy, J., Sengupta, K., Frege, C., Gordon, H., Williamson, C., Heinritzi,
774   M., Simon, M., Yan, C., Almeida, J., Tröstl, J., Nieminen, T., Ortega, I. K., Wagner, R.,
775   Adamov, A., Amorim, A., Bernhammer, A.-K., Bianchi, F., Breitenlechner, M., Brilke,
776   S., Chen, X., Craven, J., Dias, A., Ehrhart, S., Flagan, R. C., Franchin, A., Fuchs, C.,
777   Guida, R., Hakala, J., Hoyle, C. R., Jokinen, T., Junninen, H., Kangasluoma, J., Kim,
778   J., Krapf, M., Kürten, A., Laaksonen, A., Lehtipalo, K., Makhmutov, V., Mathot, S.,
779   Molteni, U., Onnela, A., Peräkylä, O., Piel, F., Petäjä, T., Praplan, A. P., Pringle, K.,
780   Rap, A., Richards, N. A. D., Riipinen, I., Rissanen, M. P., Rondo, L., Sarnela, N.,
781   Schobesberger, S., Scott, C. E., Seinfeld, J. H., Sipilä, M., Steiner, G., Stozhkov, Y.,
782   Stratmann, F., Tomé, A., Virtanen, A., Vogel, A. L., Wagner, A. C., Wagner, P. E.,
783   Weingartner, E., Wimmer, D., Winkler, P. M., Ye, P., Zhang, X., Hansel, A., Dommen,
784   J., Donahue, N. M., Worsnop, D. R., Baltensperger, U., Kulmala, M., Carslaw, K. S.,
785   and Curtius, J.: Ion-induced nucleation of pure biogenic particles, Nature, 533, 521–
786   526, https://doi.org/10.1038/nature17953, 2016.

787   Koenig, A. M., Magand, O., Laj, P., Andrade, M., Moreno, I., Velarde, F., Salvatierra,
788   G., Gutierrez, R., Blacutt, L., Aliaga, D., Reichler, T., Sellegri, K., Laurent, O., Ramonet,
789   M., and Dommergue, A.: Seasonal patterns of atmospheric mercury in tropical South
790   America as inferred by a continuous total gaseous mercury record at Chacaltaya station
791   (5240 m) in Bolivia, Atmos. Chem. Phys., 21, 3447–3472, https://doi.org/10.5194/acp-
792   21-3447-2021, 2021.

793   Komppula, M., Vana, M., Kerminen, V.-M., Lihavainen, H., Viisanen, Y., Horrak, U.,
794   Komsaare, K., Tamm, E., Hirsikko, A., and Laakso, L.: Size distributions of
795   atmospheric ions in the Baltic Sea region, Boreal Env, Res, 12, 323–336, 2007.

796   Kosyakov, D. S., Ul'yanovskii, N. V., Latkin, T. B., Pokryshkin, S. A., Berzhonskis, V.
797   R., Polyakova, O. V., and Lebedev, A. T.: Peat burning – An important source of
798   pyridines in the earth atmosphere, Environ. Pollut., 266, 115109,
799   https://doi.org/10.1016/j.envpol.2020.115109, 2020.

800   Kulmala, M., Dal Maso, M., Mäkelä, J. M., Pirjola, L., Väkevä, M., Aalto, P.,
801   Miikkulainen, P., Hämeri, K., and O'Dowd, C. D.: On the formation, growth and
802   composition of nucleation mode particles, Tellus Ser. B Chem. Phys. Meteorol., 53,
803   479–490, https://doi.org/10.3402/tellusb.v53i4.16622, 2001.

804   Kürten, A., Rondo, L., Ehrhart, S., and Curtius, J.: Calibration of a Chemical Ionization
805   Mass Spectrometer for the Measurement of Gaseous Sulfuric Acid, J. Phys. Chem. A,
806   116, 6375–6386, https://doi.org/10.1021/jp212123n, 2012.

807   Lee, S.-H., Reeves, J. M., Wilson, J. C., Hunton, D. E., Viggiano, A. A., Miller, T. M.,
808   Ballenthin, J. O., and Lait, L. R.: Particle Formation by Ion Nucleation in the Upper
809   Troposphere and Lower Stratosphere, Science, 301, 1886–1889,
810   https://doi.org/10.1126/science.1087236, 2003.

811   Lloyd, S. P.: Least Squares Quantization in PCM, IEEE Trans. Inf. Theory, 28, 129–
812   137, https://doi.org/10.1109/TIT.1982.1056489, 1982.

813   Manninen, H. E., Nieminen, T., Asmi, E., Gagné, S., Häkkinen, S., Lehtipalo, K., Aalto,
814   P., Vana, M., Mirme, A., Mirme, S., Hõrrak, U., Plass-Dülmer, C., Stange, G., Kiss, G.,
815   Hoffer, A., Törő, N., Moerman, M., Henzing, B., de Leeuw, G., Brinkenberg, M.,
816   Kouvarakis, G. N., Bougiatioti, A., Mihalopoulos, N., O'Dowd, C., Ceburnis, D.,
817   Arneth, A., Svenningsson, B., Swietlicki, E., Tarozzi, L., Decesari, S., Facchini, M. C.,
818   Birmili, W., Sonntag, A., Wiedensohler, A., Boulon, J., Sellegri, K., Laj, P., Gysel, M.,
819   Bukowiecki, N., Weingartner, E., Wehrle, G., Laaksonen, A., Hamed, A., Joutsensaari,
820   J., Petäjä, T., Kerminen, V.-M., and Kulmala, M.: EUCAARI ion spectrometer
821   measurements at 12 European sites – analysis of new particle formation events, Atmos.
822   Chem. Phys., 10, 7907–7927, https://doi.org/10.5194/acp-10-7907-2010, 2010.

823   Martin, R. V., Sauvage, B., Folkins, I., Sioris, C. E., Boone, C., Bernath, P., and Ziemke,
824   J.: Space-based constraints on the production of nitric oxide by lightning, J. Geophys.
825   Res. Atmos., 112, https://doi.org/10.1029/2006JD007831, 2007.

826   Mirme, S. and Mirme, A.: The mathematical principles and design of the NAIS - A
827   spectrometer for the measurement of cluster ion and nanometer aerosol size
828   distributions, Atmos. Meas. Tech., 6, 1061–1071, https://doi.org/10.5194/AMT-6-
829   1061-2013, 2013.

830   Moussallam, Y., Tamburello, G., Peters, N., Apaza, F., Schipper, C. I., Curtis, A.,
831   Aiuppa, A., Masias, P., Boichu, M., Bauduin, S., Barnie, T., Bani, P., Giudice, G., and
832   Moussallam, M.: Volcanic gas emissions and degassing dynamics at Ubinas and
833   Sabancaya volcanoes; implications for the volatile budget of the central volcanic zone,
834   J. Volcanol. Geotherm. Res., 343, 181–191, https://doi.org/10/gbz77j, 2017.

835   Ravi Kumar, M., Prabhakar, S., Nagaveni, V., and Vairamani, M.: Estimation of gas-
836   phase acidities of a series of dicarboxylic acids by the kinetic method, Rapid Commun.
837   Mass Spectrom., 19, 1053–1057, https://doi.org/10.1002/rcm.1888, 2005.

838   Rose, C., Sellegri, K., Velarde, F., Moreno, I., Ramonet, M., Weinhold, K., Krejci, R.,
839   Ginot, P., Andrade, M., Wiedensohler, A., Laj, P., Rose, B. C., Sellegri, K., Velarde, F.,
840   Moreno, I., Ramonet, M., Weinhold, K., Krejci, R., Ginot, P., Andrade, M.,
841   Wiedensohler, A., and Laj, P.: Frequent nucleation events at the high altitude station of

842   Chacaltaya (5240 m a.s.l.), Bolivia, Atmos. Environ., 102, 18–29,
843   https://doi.org/10.1016/j.atmosenv.2014.11.015, 2015.

844   Rose, C., Sellegri, K., Moreno, I., Velarde, F., Ramonet, M., Weinhold, K., Krejci, R.,
845   Andrade, M., Wiedensohler, A., Ginot, P., and Laj, P.: CCN production by new particle
846   formation in the free troposphere, Atmos. Chem. Phys., 17, 1529–1541,
847   https://doi.org/10.5194/acp-17-1529-2017, 2017.

848   Rose, C., Zha, Q., Dada, L., Yan, C., Lehtipalo, K., Junninen, H., Mazon, S. B., Jokinen,
849   T., Sarnela, N., Sipilä, M., Petäjä, T., Kerminen, V.-M., Bianchi, F., and Kulmala, M.:
850   Observations of biogenic ion-induced cluster formation in the atmosphere, Sci. Adv., 4,
851   eaar5218, https://doi.org/10.1126/sciadv.aar5218, 2018.

852   Schobesberger, S., Franchin, A., Bianchi, F., Rondo, L., Duplissy, J., Kürten, A., Ortega,
853   I. K., Metzger, A., Schnitzhofer, R., Almeida, J., Amorim, A., Dommen, J., Dunne, E.
854   M., Ehn, M., Gagné, S., Ickes, L., Junninen, H., Hansel, A., Kerminen, V.-M., Kirkby,
855   J., Kupc, A., Laaksonen, A., Lehtipalo, K., Mathot, S., Onnela, A., Petäjä, T., Riccobono,
856   F., Santos, F. D., Sipilä, M., Tomé, A., Tsagkogeorgas, G., Viisanen, Y., Wagner, P. E.,
857   Wimmer, D., Curtius, J., Donahue, N. M., Baltensperger, U., Kulmala, M., and Worsnop,
858   D. R.: On the composition of ammonia–sulfuric-acid ion clusters during aerosol particle
859   formation, Atmos. Chem. Phys., 15, 55–78, https://doi.org/10/f6wwnv, 2015.

860   Schulte, P. and Arnold, F.: Pyridinium ions and pyridine in the free troposphere,
861   Geophys. Res. Lett., 17, 1077–1080, https://doi.org/10.1029/GL017i008p01077, 1990.

862   Shuman, N. S., Hunton, D. E., and Viggiano, A. A.: Ambient and Modified Atmospheric
863   Ion Chemistry: From Top to Bottom, Chem. Rev., 115, 4542–4570,
864   https://doi.org/10.1021/cr5003479, 2015.

865   Sims, G. K., O'Loughlin, E. J., and Crawford, R. L.: Degradation of pyridines in the
866   environment, Crit. Rev. Environ. Control, 19, 309–340,
867   https://doi.org/10.1080/10643388909388372, 1989.

868   Skamarock, W. C., Klemp, J. B., Dudhia, J., Gill, D. O., Liu, Z., Berner, J., Wang, W.,
869   Powers, J. G., Duda, M. G., Barker, D. M., and Huang, X.-Y.: A Description of the
870   Advanced Research WRF Model Version 4, UCAR/NCAR,
871   https://doi.org/10.5065/1DFH-6P97, 2019.

872   Smith, D. and Spanel, P.: Ions in the terrestrial atmosphere and in interstellar clouds,
873   Mass Spectrom. Rev., 14, 255–278, https://doi.org/10/frmkdk, 1995.

874   Venzac, H., Sellegri, K., Laj, P., Villani, P., Bonasoni, P., Marinoni, A., Cristofanelli, P.,
875   Calzolari, F., Fuzzi, S., Decesari, S., Facchini, M.-C., Vuillermoz, E., and Verza, G. P.:
876   High frequency new particle formation in the Himalayas, Proc. Natl. Acad. Sci., 105,
877   15666–15671, https://doi.org/10/drcwqj, 2008.

878   Wang, X.-B., Nicholas, J. B., and Wang, L.-S.: Photoelectron Spectroscopy and

879   Theoretical Calculations of SO4- and HSO4-: Confirmation of High Electron Affinities
880   of SO4 and HSO4, J. Phys. Chem. A, 104, 504–508, https://doi.org/10.1021/jp992726r,
881   2000.

882   Wiedensohler, A., Birmili, W., Nowak, A., Sonntag, A., Weinhold, K., Merkel, M.,
883   Wehner, B., Tuch, T., Pfeifer, S., Fiebig, M., Fjäraa, A. M., Asmi, E., Sellegri, K., Depuy,
884   R., Venzac, H., Villani, P., Laj, P., Aalto, P., Ogren, J. A., Swietlicki, E., Williams, P.,
885   Roldin, P., Quincey, P., Hüglin, C., Fierz-Schmidhauser, R., Gysel, M., Weingartner, E.,
886   Riccobono, F., Santos, S., Grüning, C., Faloon, K., Beddows, D., Harrison, R.,
887   Monahan, C., Jennings, S. G., O'Dowd, C. D., Marinoni, A., Horn, H.-G., Keck, L.,
888   Jiang, J., Scheckman, J., McMurry, P. H., Deng, Z., Zhao, C. S., Moerman, M., Henzing,
889   B., de Leeuw, G., Löschau, G., and Bastian, S.: Mobility particle size spectrometers:
890   harmonization of technical standards and data structure to facilitate high quality long-
891   term observations of atmospheric particle number size distributions, Atmos. Meas.
892   Tech., 5, 657–685, https://doi.org/10.5194/amt-5-657-2012, 2012.

893   Wiedensohler, A., Andrade, M., Weinhold, K., Müller, T., Birmili, W., Velarde, F.,
894   Moreno, I., Forno, R., Sanchez, M. F., Laj, P., Ginot, P., Whiteman, D. N., Krejci, R.,
895   Sellegri, K., and Reichler, T.: Black carbon emission and transport mechanisms to the
896   free troposphere at the La Paz/El Alto (Bolivia) metropolitan area based on the Day of
897   Census   (2012),   Atmos.   Environ.,   194,   158–169,
898   https://doi.org/10.1016/j.atmosenv.2018.09.032, 2018.

899   Williams, E. R.: The global electrical circuit: A review, Atmos. Res., 91, 140–152,
900   https://doi.org/10.1016/j.atmosres.2008.05.018, 2009.

901   Wilson, C. T. R.: On a method of making visible the paths of ionising particles through
902   a gas, Proc. R. Soc. Lond. Ser. Contain. Pap. Math. Phys. Character, 85, 285–288,
903   https://doi.org/10.1098/rspa.1911.0041, 1911.

904   Yan, C., Dada, L., Rose, C., Jokinen, T., Nie, W., Schobesberger, S., Junninen, H.,
905   Lehtipalo, K., Sarnela, N., Makkonen, U., Garmash, O., Wang, Y., Zha, Q., Paasonen,
906   P., Bianchi, F., Sipilä, M., Ehn, M., Petäjä, T., Kerminen, V. M., Worsnop, D. R., and
907   Kulmala, M.: The role of H2SO4-NH3 anion clusters in ion-induced aerosol nucleation
908   mechanisms in the boreal forest, Atmos. Chem. Phys., 18, 13231–13243,
909   https://doi.org/10.5194/acp-18-13231-2018, 2018.

910   Yu, F.: Ion-mediated nucleation in the atmosphere: Key controlling parameters,
911   implications, and look-up table, J. Geophys. Res. Atmos., 115,
912   https://doi.org/10.1029/2009JD012630, 2010.

913   Zha, Q., Yan, C., Junninen, H., Riva, M., Sarnela, N., Aalto, J., Quéléver, L., Schallhart,
914   S., Dada, L., Heikkinen, L., Peräkylä, O., Zou, J., Rose, C., Wang, Y., Mammarella, I.,
915   Katul, G., Vesala, T., Worsnop, D. R., Kulmala, M., Petäjä, T., Bianchi, F., and Ehn, M.:
916   Vertical characterization of highly oxygenated molecules (HOMs) below and above a
917   boreal   forest   canopy,   Atmos.   Chem.   Phys.,   18,   17437–17450,

918   https://doi.org/10.5194/acp-18-17437-2018, 2018.

919   Zha, Q.: Figure data of "Measurement report: Molecular-level investigation of
920   atmospheric cluster ions at the tropical high-altitude research station Chacaltaya (5240
921   m a.s.l.) in the Bolivian Andes", https://doi.org/10.5281/zenodo.7271286, [Data set].
922   Zenodo., 2022.